

Deep Transfer Learning-Based Broken Rotor Fault Diagnosis For Induction Motors

Fırat DİŞLİ^{1*}, Mehmet GEDİKPİNAR², Abdulkadir ŞENGÜR³

^{1,2,3} Electrical and Electronics Engineering Department, Technology Faculty, Firat University, Elâziğ, Turkey

^{*1} dislifirat@gmail.com, ² mgedikpinar@gmail.com, ³ ksengur@gmail.com

(Geliş/Received: 08/03/2023;

Kabul/Accepted:21/03/2023)

Abstract: Due to their starting and running torque needs as well as their four-quadrant operation, modern industrial drives utilise induction motors (IM). Failures in the rotor bars of the motor can be found using the voltages and currents of each of the three phases as well as the acceleration and velocity signals. For the diagnosis of the quantity of broken rotor bars for a failed IM, conventional signal processing-based feature extraction techniques and machine learning algorithms have been applied in the past. The number of broken rotor bars is determined in this study by looking into a novel technique. For the aforementioned aims, specifically, the deep learning methodologies are studied. In order to do this, convolutional neural network (CNN) transfer learning algorithms are described. Initially, a bandpass filter is used for denoising, and then the signals are transformed using the continuous wavelet transform to create time-frequency pictures (CWT). The collected images are used for deep feature extraction and classification using the support vector machine (SVM) classifier, as well as for fine-tuning the pre-trained ResNet18 model. Metrics for performance evaluation employ categorization accuracy. Additionally, the results demonstrate that the deep features that are recovered from the mechanical vibration signal and current signal yield the greatest accuracy score of 100%. Nonetheless, a performance comparison with the publicly available techniques is also done. The comparisons also demonstrate that the proposed strategy outperforms the compared methods in terms of accuracy scores.

Key words: Broken Rotor Bars, Deep Learning, Continuous Wavelet Transform, Convolutional Neural Network, Induction Motor, Support Vector Machine.

Asenkron Motor Kırık Rotor Çubuğu Arızasının Derin Transfer Öğrenme Tabanlı Teşhis

Öz: Modern endüstriyel sürücüler, başlatma ve çalıştırma torku gereksinimleri ve dört bölge çalışabilmesi nedeniyle asenkron motorlarını kullanırlar. Üç fazın her birinin gerilimleri ve akımları ile titreşim sinyalleri, motorun rotor çubuklarındaki arızaları belirlemek için kullanılabilir. Literatürde, arızalı bir asenkron motorun kırık rotor çubuklarının sayısını teşhis etmek için geleneksel sinyal işleme tabanlı özellik çıkarma yaklaşımları ve makine öğrenimi algoritmaları kullanılmaktadır. Bu çalışmada, kırık rotor çubuklarının sayısının belirlenmesi için yeni bir algoritma önerilmiştir. Spesifik olarak, belirtilen amaçlar için derin öğrenme yaklaşımları incelenmiştir. Bu amaçla, evrişimli sinir ağı (CNN) üzerinde transfer öğrenme yaklaşımı sunulmaktadır. Arıza teşhisi için motorun titreşim sinyali ve bir faz akım sinyali kullanılmıştır. Gürültü giderme için, başlangıçta bir bant geçiren filtre kullanılmış ve daha sonra sürekli dalgacık dönüşümü (CWT) kullanılarak sinyaller zaman-frekans görüntülerine dönüştürülmüştür. Elde edilen görüntüler ile önceden eğitilmiş ResNet18 modelinin ince ayarı kullanılarak derin öznetelik çıkarımı yapılmış ve destek vektör makinesi (SVM) sınıflandırıcısı ile de arıza sınıflandırması yapılmıştır. Sınıflandırma doğruluğu, performans değerlendirme ölçütleri için kullanılmış ve yapılan deneyler ile mekanik titreşim sinyali ve akım sinyalinden çıkarılan derin öznetelikler ile en yüksek doğruluk puanının %100 ile elde edildiğini göstermektedir. Öte yandan, yayınlanan yaklaşımlarla bir performans karşılaştırması da yapılmaktadır. Son olarak, karşılaştırmalar, önerilen yöntemin karşılaştırılan yöntemlerden daha iyi doğruluk puanları ürettiğini göstermektedir.

Anahtar kelimeler: Asenkron Motor, Derin Öğrenme, Destek Vektör Makinesi, Evrişimli Sinir Ağı, Kırık Rotor Çubuğu

1. Introduction

Induction motors (IMs) are frequently used in modern industry because of their high efficiency, low cost, and high starting torque [1]. Since IMs are the main movement providers in many fields such as mining, transportation, and textile, the working conditions of IMs affect the whole work process [2]. For this reason, condition monitoring and condition-based maintenance are required in IMs. Although IMs are robust machines, faults inevitably occur in these motors. Common fault types in these motors are bearing, broken rotor bars, and winding faults. According to the studies in the literature, rotor bar failure accounts for 9% of total failures. While the rotor bars start to fail as small cracks, they become completely broken over time. With these failures, the motors start to work with vibration and noise, and thus, a decrease in efficiency takes place. In progressive failure levels, the motors become inoperable and undesirable situations emerge in the system [1-4].

* Corresponding author: dislifirat@gmail.com. ORCID Number of authors: ¹ 0000-0003-0016-3558, ² 0000-0002-1045-7384, ³ 0000-0003-1614-2639

Using stator current or monitoring motor vibration signals is at the forefront in detecting rotor bar failure which is common in IMs. In addition, current and vibration signals are analyzed by using signal processing techniques such as FFT (fast fourier transform) and DWT (discrete wavelet transform). Recently, with the increase in the computational capabilities of computers, fault detection and diagnosis has gained importance by using artificial neural network, machine learning, and deep learning algorithms as well as signal processing techniques [2,28-31].

Kumar et al. proposed dilated CNN-based method for bearing and broken rotor bar failure diagnosis. They converted the vibration signals obtained from the IM into images using wavelet decomposition and then they classified them with dilated CNN. They reached an accuracy of 99.5% in their study [1]. Taher et al. created a defective motor model using FEM (finite element method) and Matlab. They first applied notch filter and then DWT to the current signals obtained from the model. Using the 6th and 7th levels of the detail coefficients obtained as a result of the DWT, they stated that these two levels could be used in the diagnosis of rotor bar failure [2]. Mustafa et al. applied Park transform to the current and voltage signals of the failed motor to diagnose the broken rotor bar failure and created a Fault Diagram using the Set Membership Identification method from the I_q and V_q components [3]. Heider et al. proposed an EPFA-based algorithm for rotor failure diagnosis. In their study, both synthetically produced and stator current signals obtained from FEM were used [4]. Shi et al. have run their method for diagnosing the magnitude of rotor bar failure in a 3-phase IM on a dynamic model of the motor and tested it on a real motor. The main idea of their work was to generate a fault index by using an arithmetic mean and standard deviation and these values were obtained from WT-applied stator current [5]. Aydin et al., applied Hilbert transform and MCSA (motor current signature analysis) techniques to the stator current signal to determine the number of broken rotor bars [6]. Sabir et al., using DWT and ETSA (electrical time synchronous averaging) from the current signals obtained from the rotor failure experiment set they created, found the rotor failure frequency range and classified the failure with Fuzzy Logic [7]. Bessam et al. created a broken rotor bar failure test set and performed tests at different loads in order to determine the number of broken rotor bars. By applying the Hilbert transform and FFT to the stator current, harmonics were obtained. They classified the number of broken rotor bars with the NN (neural network) they created using the position and amplitude of these harmonics [8]. Singh et al. created an experimental set with a half-broken rotor bar for the detection of broken rotor bars in an IM at the initial stages. They diagnosed the rotor failure at the initial stages by using the current signals obtained from the experimental set, using MCSA and MUSIC (multiple signal classification) [9]. Ameid et al. have attempted a sensorless diagnostic based on FOC (field oriented control) for rotor failure of a vector-controlled IM. For this purpose, a Matlab model and experimental set of the failed IM were created. By applying DWT to the current signal, they detected the fault with the energy levels of the sidebands of the signal. In addition, they used a driver to compensate for the effect of the fault on the speed during operation [10]. Quiroz et al. performed rotor failure diagnosis in the LS-PMSM (line start permanent magnet synchronous motor) transient state. Although MCSA is difficult in the transient state of the motor, this analysis was performed in the transient state since current flows through the rotor bars in the LS-PMSMs in the transient state. The 13 most important features of the stator current signals obtained from healthy and faulty motors were extracted with Statical Time Domain Features and classified with the help of the Random Forest algorithm. In the second case, they re-run their models with 2 of the most important features (Features Importance) and classified them. They asserted that they achieved success by 98.8% when they used 13 features and 98.4% with 2 features [11].

Gandhi et al. generated abnormal gear teeth and broken rotor bar failure both experimentally and in simulation software (Matlab/Simulink). They developed two models based on PSO (particle swarm optimization) and MPSO (modified PSO) and tested these models in their simulation and experimental systems. In their study, they concluded that the increase in fault density became noticeable from the frequency characteristic [12]. On the other hand, Rangel-Magdalenos et al. used 3mm 5mm 7mm and 10mm drilled rotors to diagnose different levels of broken rotor failure. They calculated the Kurtosis value after using the current signal EMD (empirical mode decompose) of a healthy and damaged motor at different levels and applying Hilbert transform to each of its IMFs (intrinsic mode functions). Afterwards, they showed that it was possible to detect the fault status of the motor with the Kurtosis value they obtained [13].

Differently, Malek et al. constructed a Matlab model of the motor to determine the exact location of the broken rotor bar. The stator currents were obtained by starting the motor both directly and with the help of an inverter. Then, they applied Hilbert Transform to the stator currents and determined the exact position of the broken rotor bar with the algorithm they developed [14]. Furthermore, Halder et al. have diagnosed the broken rotor failure by doing the transient analysis of the IM. Firstly, they used both FEM and open-source IM data. Secondly, they analyzed the stator current by applying STFT (short time fourier transform) and Inverse Thresholding techniques [15]. Similarly, Liu et al. created a 2-bar broken dynamic model of the motor using the

multi-loop equivalent circuit of the rotor in Matlab. They analyzed the stator current obtained from the model with both the Compressive Sensing method and MCSA and deduced the fault characteristics of the motor. In their study, they asserted that fault diagnosis could be made quickly with the Compressive Sensing technique [16]. Georgulas et al. applied PCA (Principle Component Analysis) to the stator current for broken rotor failure in a 3-phase IM and classified the obtained components with HMM (Hidden Markov Models). According to them, the combination of PCA and HMM was successful in fault diagnosis [17]. Lastly, Khater et al. determined the number of broken bars in the rotor depending on the rotor resistance change. Since the rotor resistance could not be measured directly, the data obtained with the torque meter and angular speedometer was successfully determined with the help of some formulas [18].

This study uses a brand-new method for identifying damaged rotor bars. For the aforementioned aims, specifically, deep learning methodologies are studied. The illustration of the proposed method is given in Figure. 1. To do this, convolutional neural network (CNN) transfer learning algorithms are described. Utilized are the radial mechanical vibration speeds on the driven side signal and the current signal.

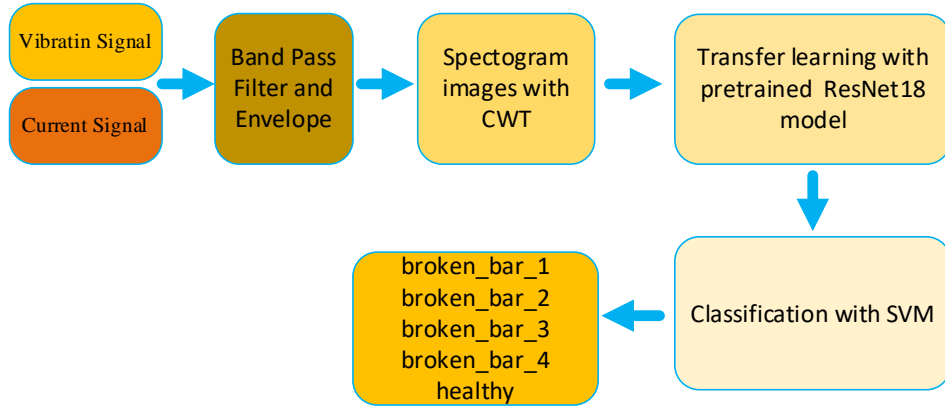


Figure. 1 Proposed methodology

First, a bandpass filter is used to denoise the signals, and then a continuous wavelet transform is used to turn the data into time-frequency pictures (CWT). The collected pictures are used for the support vector machine (SVM) classifier's deep feature extraction and classification as well as for fine-tuning the pretrained ResNet18 model. The performance evaluation metric is classification accuracy. The results of the trials demonstrate that the deep features derived from the mechanical vibration signal and current signal yield the greatest accuracy score of 100%. There is also a performance comparison with the methods that have been published. The comparisons indicate that the suggested technique outperforms the competing methods regarding accuracy scores.

2. Theoretical Background

2.1. Broken Rotor Bar

By observing the distinctive harmonic components (f_{BRB}) in the stator line-current and vibration signal, it is possible to detect induction motor broken-rotor-bars (BRB) in steady-state [10]. These frequencies in the current signal are defined as follows,

$$f_{BRB} = f_s(1 \pm 2ks) \quad (1)$$

Where k is $1, 2, 3, \dots, n$, f_s is frequency of the magnetic field and s is the rotor slip and it is calculated as:

$$s = \frac{n_s - n}{n_s} \quad (2)$$

Where n_s is synchronous speed and n is the rotor speed.

2.2. Continuous Wavelet Transform

In this section, principles related to CWT (continuous wavelet transform) are presented. Wavelet transform, abbreviated as WT, is considered an effective technique for machine diagnostics using sound, vibration and current signals, as it can be used to analyse both stationary and transient signals [19]. According to the studies, WT has certain advantages in characterizing the signal at different levels in the time and frequency domain. The principle of CWT which is a different approach to WT, can be defined as follows [20].

$$C_\psi = \int_{-\infty}^{\infty} \frac{|\hat{\psi}(f)|^2}{|f|} df < \infty \quad (3)$$

A wavelet $\psi(t)$ is a function of the zero average.

$$\int_{-\infty}^{\infty} \psi(t) dt = 0 \quad (4)$$

$\psi(t)$ is a wavelet function and $L_2(\mathbb{R})$ is the space of square-integrable functions. The corresponding wavelet family consists of a series of wavelets produced by dilation and translation from the main wavelet $\psi(t)$, this is given in equation 5.

$$\psi_{x,y} = \frac{1}{\sqrt{x}} \psi\left(\frac{t-y}{x}\right) \quad (5)$$

Here, the scale factor x , the time position y , and the energy conservation factor $1/x$ are all present. When x is little, it is possible to study higher frequency components; conversely, when x is large, it is possible to analyze lower frequency components. The basis function can be moved by y in the direction that time moves when y is a fixed value. The inner product of the L_2 norm in Hilbert space can be used to organize the CWT of the $u(t)$ signal as in equation 6.

$$W_y(x) = \langle \psi_{x,y}(t), u(t) \rangle = \frac{1}{\sqrt{x}} \int u(t) \psi_{x,y}^* dt \quad (6)$$

The complex conjugate symbol here is $*$. Both the temporal location y and the scaling factor x are dynamic. This can be explained as the dot product $\psi_{x,y}(t)$ of a set of wavelet functions and the signal $u(t)$. Wavelet coefficients, which are scale and time position functions of $W_y(x)$, are used to express CWT. This describes the relationship between the CWT and the signal's wavelet function. The wavelet function and the original signal are more comparable the higher the wavelet coefficient. This technique is computationally challenging since the scaling factor x and shift factor y in CWT are always changing. By digitizing either or both of the scale factor x or the shift factor y , complexity can be decreased. As a result, various wavelet transform types are created. A binary wavelet transform is what is used, for instance, when the scale factor is binary discrete but the shift factor is continuous [20].

For a discrete array u_m , $t = m\delta t$ and $y = n\delta t$, where $m, n=0,1,2,\dots, N-1$, N is the sampling point and δt is the sampling interval. The CWT of u_m is defined as follows,

$$W_n(x_j) = \sum_{m=0}^{N-1} u_m \psi^* \left[\frac{(m-n)\delta t}{x_j} \right] \quad (7)$$

By varying the index j and n corresponding to the x scale factor and y duration, respectively, a picture of both the scale versus amplitude of any feature and how that amplitude changes over time can be constructed. Thus, $W_x(x_j)$, where the u_m function is performed by a CWT, can be viewed as an arbitrary time-frequency domain of the original signal [20].

2.3. ResNet

Residual Networks (ResNet) are convolutional networks developed to deal with vanishing and exploding gradient problems. For a more superficial model, layers added to its deeper counterpart are called identity mapping. ResNet implements a residual module, as shown in Figure. 2, which allows each stacked layer to learn a residual mapping [21].

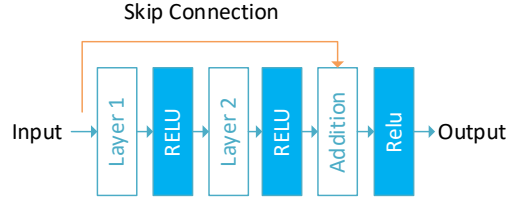


Figure 2. Schematic of a ResNet module

The final result, known as the underlying mapping, can be written as $H(x)$, where x stands for the first entries in the stacked layers. Instead of enabling stacked layers to approximate to $H(x)$, the deep residual learning module permits fit mapping to $F(x) = H(x) x$. As a result, the original mapping is transformed into $F(x)+x$, which the residual module can execute as a short cut in the neural network. There are no additional parameters or computational overhead introduced by the shortcut connections $F(x) + x$ in the Residual module. Because to its simplicity in adapting to the underlying mapping, ResNet is appealing in practice [22].

Identity mapping is done by the Residual module, and the outputs of the shortcut links are combined with the outputs of the stack layers. The module can now be specified mathematically as in equation 8.

$$y = F(x, \{W_i\}) + h(x) \tag{8}$$

Here, $h(x)$ stands for the initial input vector and y for the output vector. The residual mapping function $F(x, \{W_i\})$ is fitted by stack layers. For instance, $F = \sigma W1$ if F only contains one layer and one activation layer (RELU).

In some circumstances, $h(x)$ and y have distinct dimensions. To match dimensions, a square matrix or linear projection W_s can be conducted as described in equation 9.

$$y = F(x, \{W_i\}) + W_s h(x) \tag{9}$$

Convolutional layers (CL) are the basis of ResNet and aim to reduce the number of model parameters. In CLs, the inputs evolve with multiple convolution cores and then output features are produced by the activation unit. The formula expression of these operations can be given by equation 10 [23].

$$y_j^{l+1} = f(\sum_i x_i^l * w_{ij}^l + b_j^{l+1}) \tag{10}$$

Here l represents the number of network layers, j the index of the output feature map, and i the index of the input feature map. The $*$ represents the convolution operation used for the i . feature maps x_i^l and the j . kernel w_{ij}^l in layer l . The b_j^{l+1} bias is then added to the j . feature maps in the $l + 1$ layer. Finally, f denotes the nonlinear activation function. RELU is commonly used as an activation function and can be expressed as in equation 11.

$$y = \max(0, x) \tag{11}$$

Pooling is another important operation, often used to reduce the size of the feature matrix. There are various methods such as max-pooling and average-pooling to implement this process. The equations for max-pooling and average-pooling operations are given as follows, respectively.

$$z_{ij}^k = \max x_{pq}^k (p, q \in R_{ij}) \tag{10}$$

$$z_{ij}^k = \frac{1}{|R_{ij}|} \sum x_{pq}^k (p, q \in R_{ij}) \tag{11}$$

Here z_{ij}^k represents the output from the k . feature map of the pooling operation, x_{pq}^k represents the value of the R_{ij} neuron in the pooling region.

2.4. Support Vector Machine

The SVM (support vector machine) classifier is a continuous multiple nonlinear classifier. The linear classifier, which is the original format of SVM, works with the logic of separating two sample groups that can be linearly classified in two-dimensional space with a straight line. Instances in high-dimensional space can be separated by a hyper-plane. Instead of separating using a hyper-plane, simpler decomposition can be made by mapping data in low-dimensional space to high-dimensional space. With this principle, a kernel function is used to make the samples linearly separable. In addition, the soft margin of the SVM strengthens the generalization performance. Thus, they can be used effectively for regression and classification problems. Let x_i be an input vector, y_i the corresponding outputs, so that the training set is $\{(x_1, y_1), (x_2, y_2), \dots, (x_n, y_n)\}$. Here n is the total number of samples in the training set. The purpose of SVM is to find the hyper-plane that divides it into two different $y(y=1, y=-1)$ in the training set. Hyper-plane can be considered as a linear plane and expressed as in equation 14 [24].

$$f(x) = w^T x + b \quad (14)$$

Here w and x are the vectors of a column with the same dimensions. For optimal classification, the hyper-plane must be defined. A common definition is that the optimum hyper-plane takes the greatest geometry distance γ between the hyper-plane and two different clusters, as shown in Figure. 3. Hyper-plane calculation is as in equation 15.

$$y_i(w x_i + b) \geq 1 \quad (15)$$

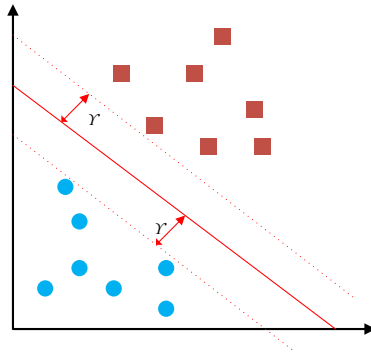


Figure 3. Geometric distance in training set

Considering the generalization performance, misclassification in SVM can be expressed by ξ_i .

$$\xi_i = \max(0, 1 - y_i (w x_i + b)) \quad (16)$$

An example of a soft variable in the classification problem is given in Figure. 4. By adding a soft variable, the optimization problem changes from equation 15 to the situation in equation 17.

$$y_i (w x_i + b) \geq 1 - \zeta_i \quad (17)$$

The kernel function is used to convert linear SVM to nonlinear. The whole problem is looking for w which is correct. w can be expressed as linear combinations.

$$w = a_1 y_1 x_1 + a_2 y_2 x_2 + \dots + a_n y_n x_n \quad (18)$$

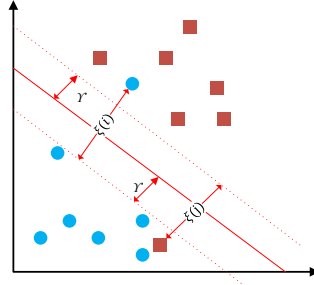


Figure 4. Soft variable of the optimization problem

In equation 18 a_i is the natural number, it is called the Lagrange Multiplier. Most of the time the Lagrange Multiplier is 0, only for minority samples, the classification determines the hyper-plane [24]. Thus, the function $f(x) = \langle w, x \rangle + b$ can be written as,

$$f(x) = \sum_{i=1}^n a_i y_i \langle x_i, x \rangle + b \quad (19)$$

2.5. Transfer Learning

Transfer learning (TF), a common and effective approach in deep learning models, is to use a pre-trained network. A pre-trained network is a neural network trained on a large dataset, typically for a large-scale classification task. Fine-tuning and Feature Extraction are common methods of using a pre-trained network. Feature Extraction is the use of representations learned by a previous network to extract meaningful features from new samples. A new classifier to be trained from scratch is added on top of the previously trained model so that the previously learned feature maps for the dataset can be reused. Fine Tuning is the training of some of the upper layers of a frozen model base with the newly added classifier after thawing. Thus, it makes the more abstract representations of the model to be reused more suitable for the problem [25].

3. Dataset

A publicly available broken rotor bar dataset has been used in our experiments. Electrical and mechanical signals from tests on three-phase IMs have been included in the dataset. Different mechanical stresses on the IM axis and various degrees of broken bar defects in the motor rotor have been tested along with data on the rotor without defects. The characteristics of the IM used in the study are 3-phase, 1-hp, 220/380V, 4 poles and a nominal speed of 1785 rpm. The dataset contains electrical and mechanical signals from experiments on three-phase IMs. The dataset contains four fault classes and one healthy class. For all classes, the dataset has been constructed with 0.5, 1.0, 1.5, 2.0, 2.5, 3.0, 3.5, and 4.0 Nm torques as the load condition. Ten experiments have been performed for each combination of healthy and loading conditions for dataset construction. The experiments were performed for the mechanical vibration speeds radial on the driven side (Vib_acpi) and the first-phase current signal (Ia) for each combination of healthy and loading conditions. The sampling frequency of vibration signals is 7600 Hz and the sampling frequency of electrical signals is 50 kHz [26].

4. Experimental Works and Results

A computer with having i7 intel microprocessor with 64 GB ram was used in experimental works. Besides, an Nvidia M4000 GPU with 8 GB ram was used for deep learning applications. All coding has been carried out with MATLAB. From the power spectrum of one of the vibration signals, Vib_acpi, observe that there are frequency components of interest in the [900 1300] Hz region. Thus, a bandpass filter was used for filtering the Vib_acpi and Ia signals, respectively. The envelope of signals after band-pass filtering was calculated. The length of signals in the dataset is 18 seconds and a non-overlapping window of length 1 second was used in 11-15 time intervals for the sampling of the envelopes of the Vib_acpi and Ia signals. Thus, a total of 2000 signal samples for each Vib_acpi and Ia signal were constructed and used in the experimental works. Figure. 5 shows the sample of the envelope of Vib_acpi signals for all classes. Besides, in Figure. 6, the envelope of the Ia current signal for all classes was given.

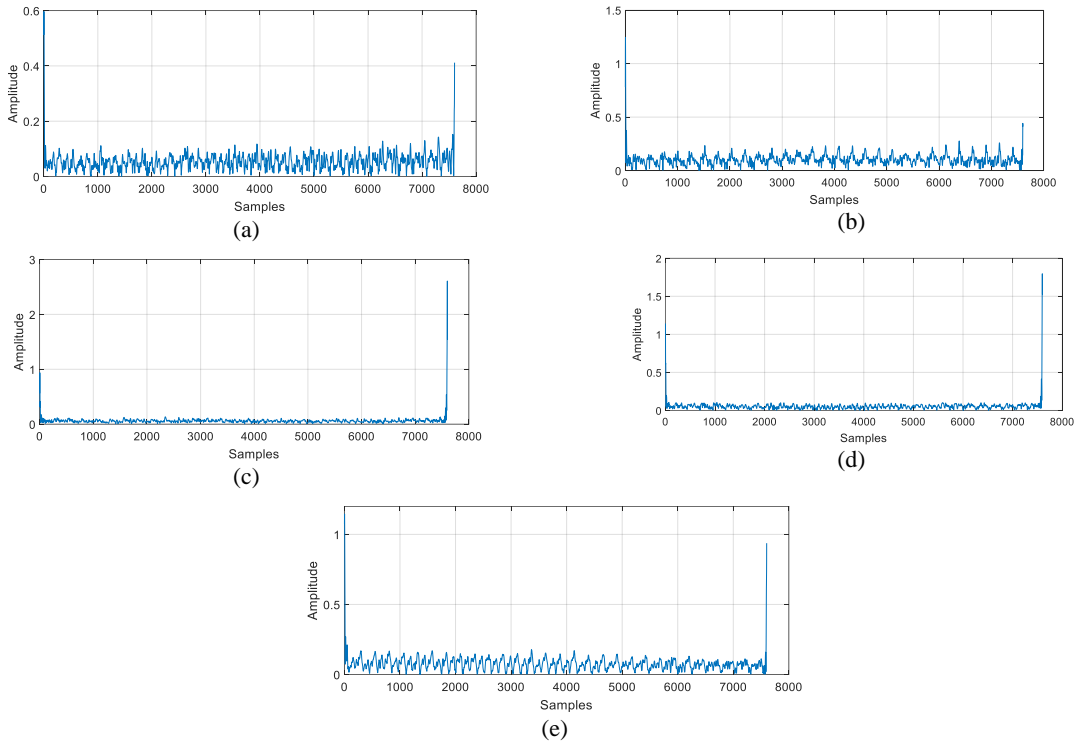


Figure 5. The envelope of the Vib_apci signals for all classes for 0.5 Nm load a) Healthy, b) One broken bar, c) Two broken bars, d) Three broken bars and e) Four broken bars

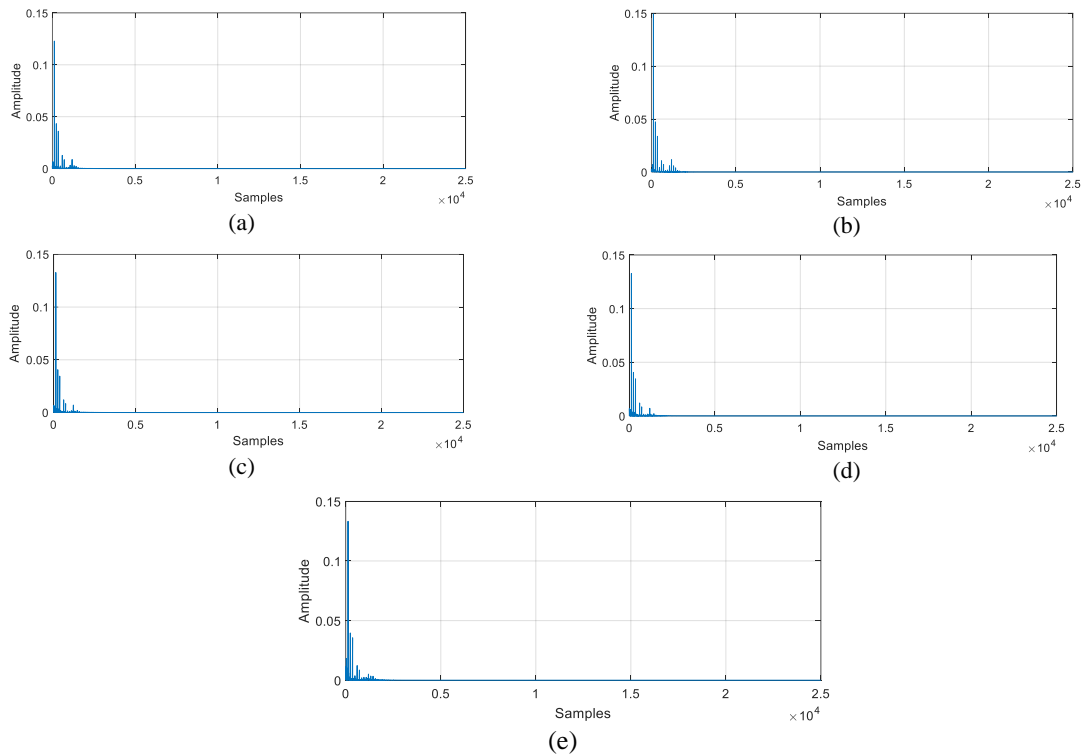


FIGURE 6. The envelope of the Ia signals for all classes for 0.5 Nm load a) Healthy, b) One broken bar, c) Two broken bars, d) Three broken bars and e) Four broken bars

Besides, Figures 7 and 8 show the time-frequency representations of the signals that were given in Figs. 2 and 3 by using the CWT. The ‘viridis’ color mapping was used in the representation of the time-frequency images.

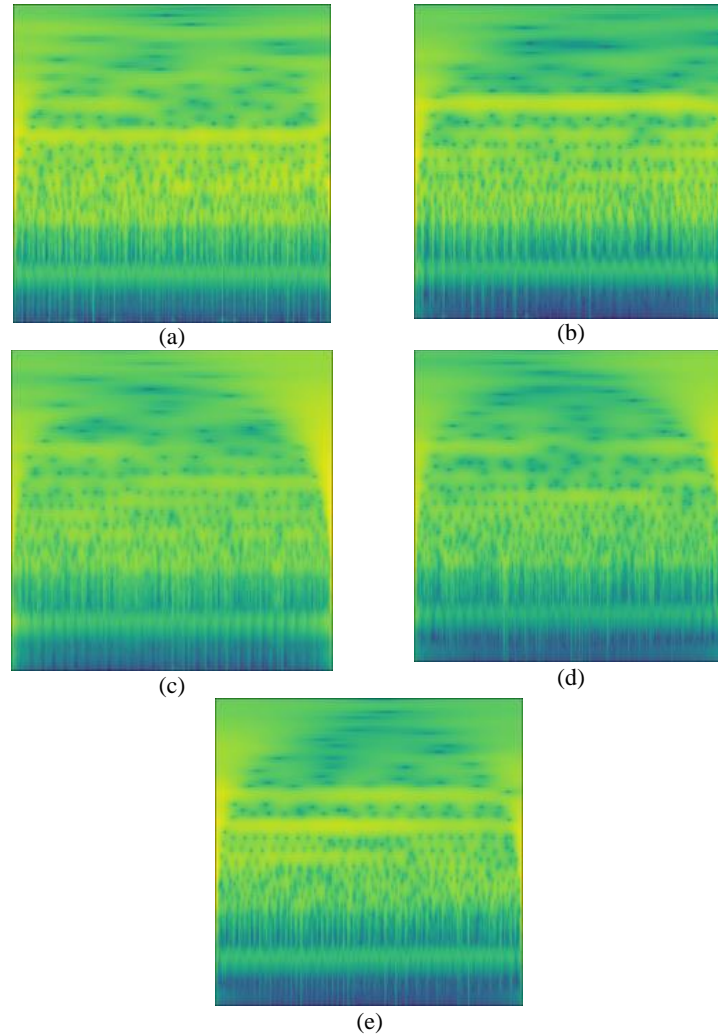


Figure 7. The time-frequency representation of the Vib_acpi signals for all classes for 0.5 Nm load a) Healthy, b) One broken bar, c) Two broken bars, d) Three broken bars and e) Four broken bars

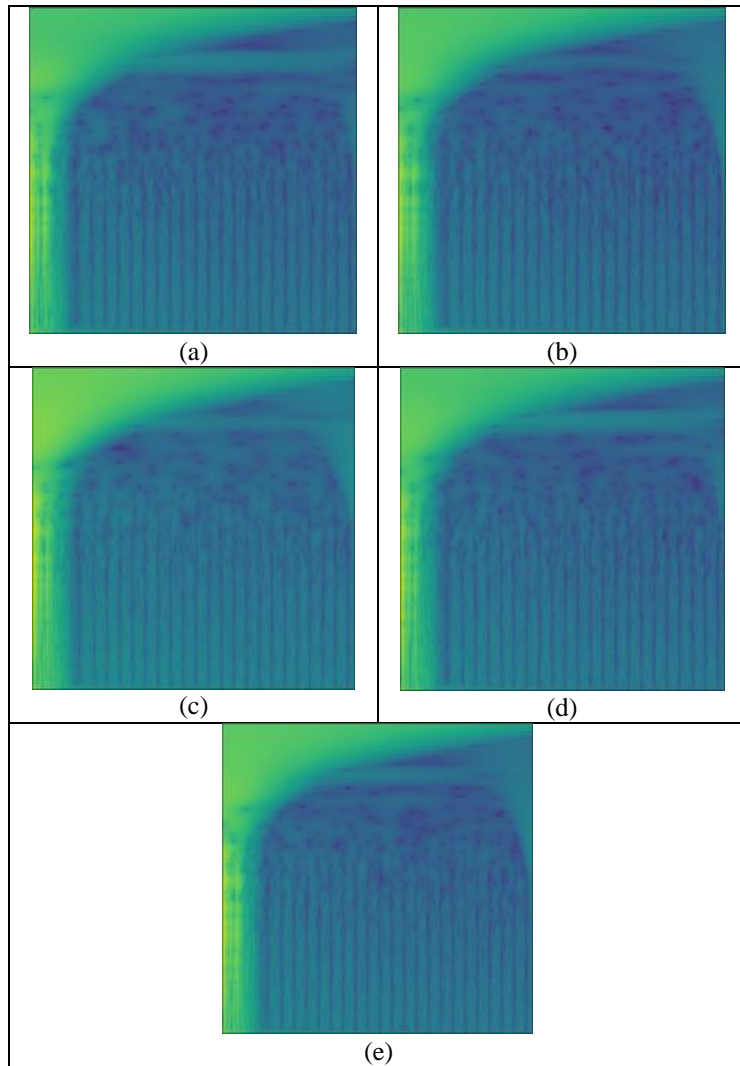


Figure 8 The time-frequency representation of the Ia signals for all classes for 0.5 Nm load a) Healthy, b) One broken bar, c) Two broken bars, d) Three broken bars and e) Four broken bars

As we investigated the achievements of the transfer learning approaches on the broken rotor bar classification problem, both deep feature extraction from the ResNet model and fine-tuning of the ResNet model was carried out. ResNet18 model was considered in experimental works due to its shallow architecture against the ResNet 50 and ResNet 101 models [22]. In deep feature extraction, the '*res3b_relu*' layer of the ResNet18 model was used and for fine-tuning, the ResNet18 model, the fully connected and classification layers were adjusted according to our mentioned problem.

The fine-tuning process was carried out with the 'sgdm' optimizer in all experiments. Figure. 9 shows the training progress of the fine-tuning of the ResNet18 model. As seen in Figure. 9, the training and validation accuracies were around 90% at the 10th epoch. And the accuracies were increased until the end of the 20th epoch. Between the 30th and 50th epochs, a bit of overfitting was observed, and the final validation accuracy was 98.00%. In Figure 10, the confusion matrix was given. In the confusion matrix, the x-axis shows the predicted classes and the y-axis shows the true classes, respectively.

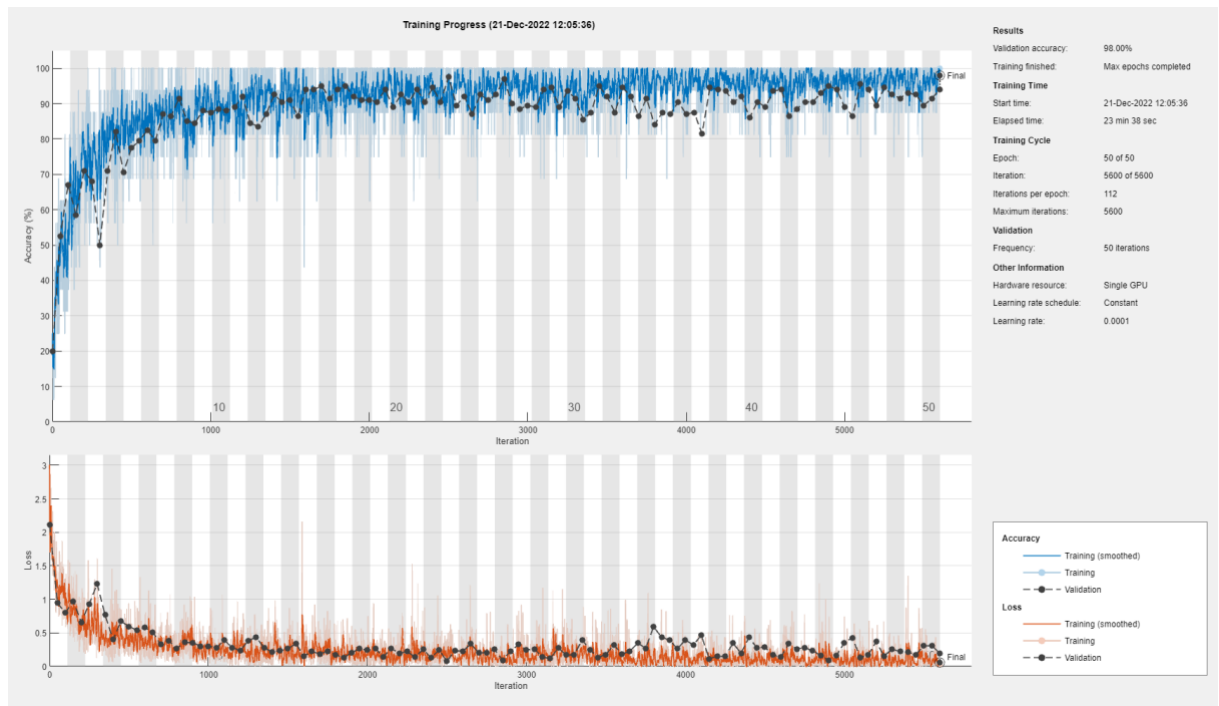


Figure 9. Result of the training progress for fine-tuning of the ResNet18 model for Ia.

As seen in Figure 10, for broken_bar_1, broken_bar_3 and healthy classes, all samples were correctly classified. For the broken_bar_2 class, only one sample was wrongly classified as broken_bar-3. Similarly, three samples from the broken_bar_4 class were classified as broken_bar_3. From this confusion matrix, it is observed that the broken_bar_3 class was confused with the broken_bar_2 and broken_bar_4 classes.

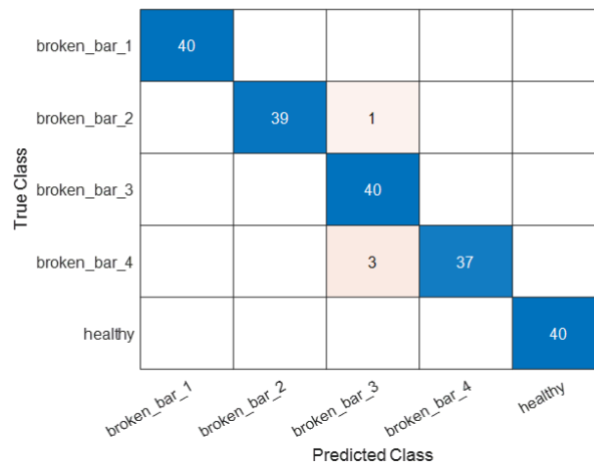


Figure 10. Confusion matrix for classification process for Ia

Figure 11 shows the training progress of the fine-tuning of the ResNet18 model for Vib_acpi. As seen in Figure 11, the training and validation accuracies were over 95% at the 10th epoch.

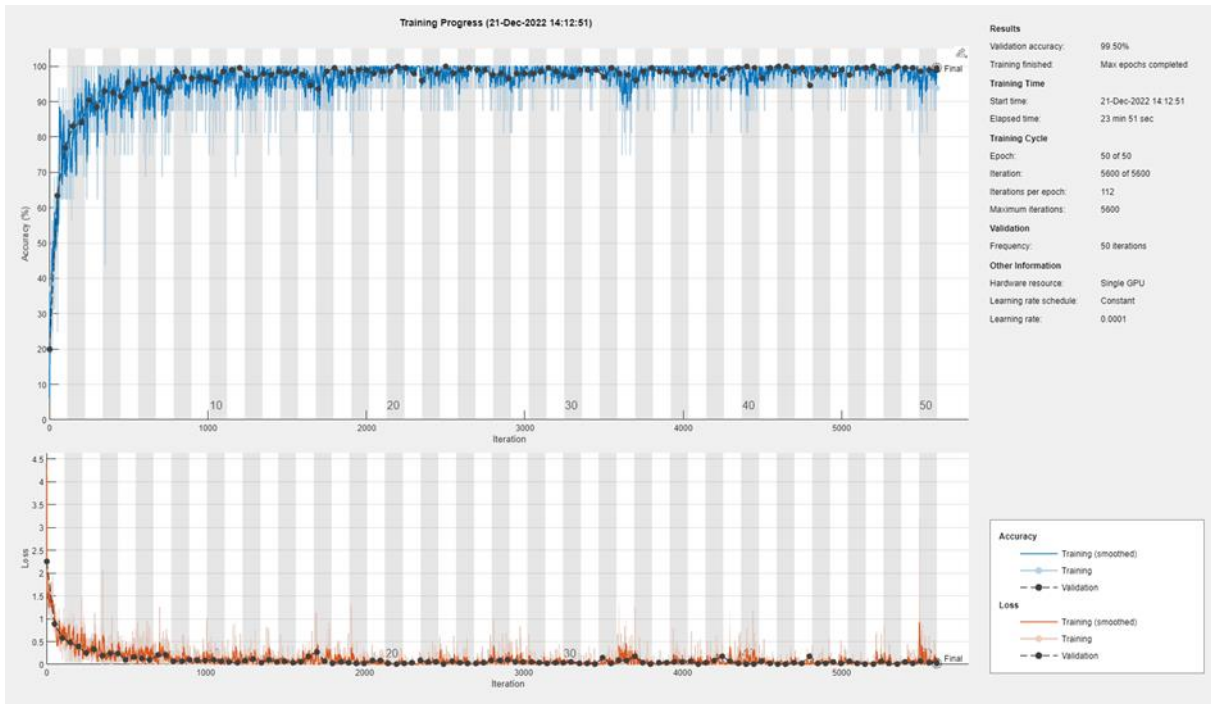


Figure 11. Result of the training progress for fine-tuning of the ResNet18 model for Vib_acpi.

And the accuracies were stable until the end of the 50th epoch. At the 15th and 33rd epochs, there have been instantaneous drops in the accuracy but in the final epoch, the accuracy was 99.50%. In Figure 12, the confusion matrix was given. As seen in Figure 12, only one sample from the healthy class was wrongly classified as broken_bar_3. And other classes were all classified with 100% accuracy scores.

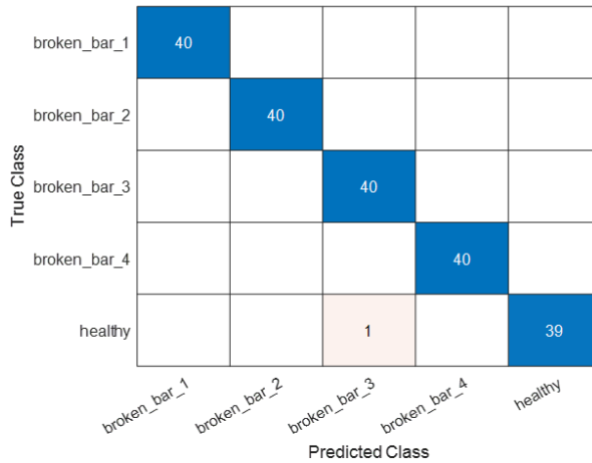


Figure 12. Confusion matrix for classification process for Vib_acpi

After fine-tuning the ResNet18 model, another experiment was carried out where deep features were extracted from the 'res3b_relu' layer and an SVM classifier was used in classification. Figure. 13 shows the obtained confusion matrix for the mentioned experiment on the Ia. As observed in Figure. 13, the overall accuracy score was 94.5%. And when this result was compared with the result that was obtained from the fine-tuning of ResNet18, a performance decrease was seen. There was a 3.5% performance decrease between these two experiments. Only the healthy class was classified with a 100% accuracy score and 2, 3, 5 and 1 samples were wrongly classified for the broken_bar_1, broken_bar_2, broken_bar_3 and broken_bar_4 classes, respectively.

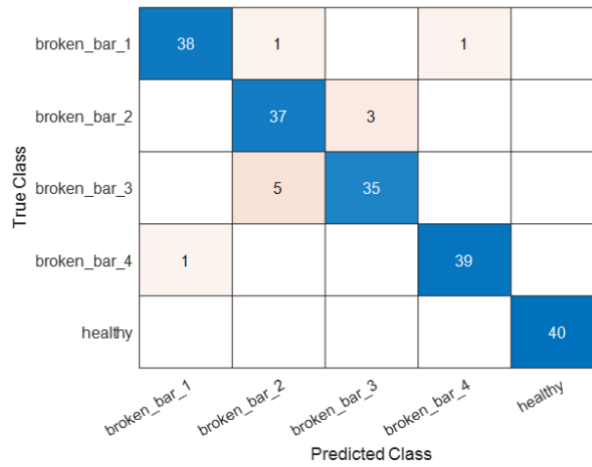


Figure 13. Confusion matrix for deep features+ SVM classification process for Ia

In Figure 14, the achievement of the deep feature extraction and SVM classification process for Vib_acpi was shown. The calculated overall accuracy score was 99% where a total of two samples from the broken_bar_3 and broken_bar_4 classes were wrongly classified. Besides, the broken_bar_1, broken_bar_2 and healthy classes were 100% correctly classified.

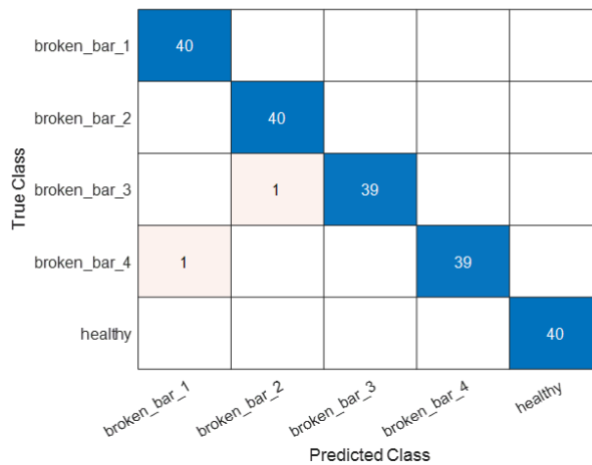


Figure 14. Confusion matrix for deep features+ SVM classification process for Vib_acpi

Lastly, a final experiment was conducted where the deep features from Vib_acpi and Ia were concatenated to form a new feature vector and the SVM classifier was used in the classification of this new feature vector. The obtained result for this experiment was shown in Figure. 15. As seen in Figure. 11, the overall classification accuracy was 100%. This accuracy score was the highest among all experiments that have been conducted in this study.

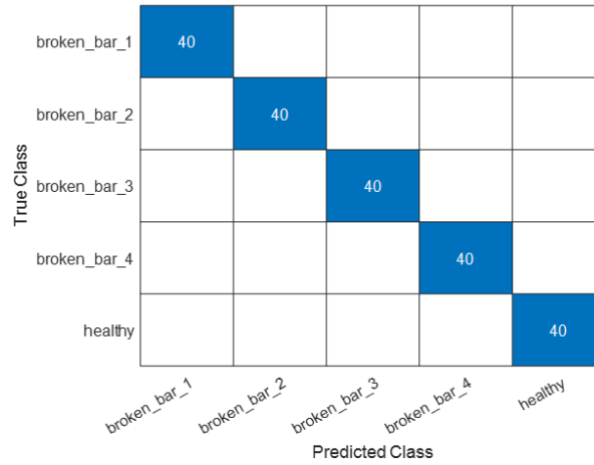


Figure 15. Confusion matrix for deep features+ SVM classification process for Vib_acpi+Ia

The comparison of the obtained results with the existing results were given in Table 1. In the compared method, time domain statistical features, and various frequency domain features were extracted and concatenated from the Vib_acpi signal. Then, one way ANOVA method was used for ranking the features for a potential feature selection operation and the first 10 to 15 features were selected and decision tree (DT) and k nearest neighbour (kNN) classifiers were used for the classification of the selected features. The identical feature extraction mechanism was also applied to the Ia signal.

Table 1. Performance comparison of the proposed method with some of the published results

	Features	Classifier	Accuracy (%)
Reference [27]	Statistical and frequency-based features by using Vib_acpi and Ia.	DT	93.8
Reference [27]	Statistical and frequency-based features by using Vib_acpi and Ia.	kNN	98.8
This study	Fine-tuning of ResNet18 on Vib_acpi	CNN	99.5
This study	Fine-tuning of ResNet18 on Ia	CNN	95.0
This study	Deep feature extraction from Vib_acpi	SVM	99.0
This study	Deep feature extraction from Ia	SVM	94.5
This study	Deep feature extraction and concatenation on Vib_acpi and Ia	SVM	100.0

As seen in Table 1, while the statistical and frequency domain features with the kNN classifier produced a 98.8% accuracy score, a 93.8% accuracy score was obtained with the identical features and DT classifier. The best accuracy score of 100% has been produced with the concatenation of the deep features and SVM classifier.

5. Conclusions

In this paper, deep transfer learning approaches are proposed for an accurate determination of the number of broken rotor bars for IMs. In the past, the general trend on such a prediction used to be based on statistical feature extraction and using a traditional machine learning approach. However, nowadays, the development of deep

learning and deep transfer learning approaches are used for the prediction of the number of broken rotor bars for IMs. Using both fine-tuning and deep feature extraction methods has been an advantage. The obtained results show that the deep learning approaches are quite efficient in the detection of the number of broken rotor bars. Especially, using the deep features, which are extracted from vibration signal and current of phase, produced the highest accuracy score that has been obtained so far.

References

- [1] Kumar P, Hati AS. Dilated convolutional neural network-based model for bearing faults and broken rotor bar detection in squirrel cage induction motors. *Expert Syst Appl* 2022;191.
- [2] Taher SA, Malekpour M, Farshadnia M. Diagnosis of broken rotor bars in induction motors based on harmonic analysis of fault components using modified adaptive notch filter and discrete wavelet transform, *Simul Model Pract Theory* 2014; 44: 26–41.
- [3] Mustafa MO, Nikolakopoulos G, Gustafsson T, Kominiak D. A fault detection scheme based on minimum identified uncertainty bounds violation for broken rotor bars in induction motors. *Control Eng Pract* 2016; 48: 63–77.
- [4] Halder S, Dora BK, Bhat S. An Enhanced Pathfinder Algorithm-based MCSA for rotor breakage detection of induction motor, *J Comput Sci* 2022;64.
- [5] Shi P, Chen Z, Vagapov Y, Zouaoui Z. A new diagnosis of broken rotor bar fault extent in three-phase squirrel cage induction motor, *Mech Syst Signal Process* 2014; 42(1–2): 388–403.
- [6] Aydin I, Karakose M, Akin E. A new method for early fault detection and diagnosis of broken rotor bars. *Energy Convers Manag* 2011; 52(4): 1790–1799.
- [7] Sabir H, Ouassaid M, Ngote N. An experimental method for diagnostic of incipient broken rotor bar fault in induction machines. *Heliyon* 2022; 8(3).
- [8] Bessam B, Menacer A, Boumehraz M, Cherif H. Detection of broken rotor bar faults in induction motor at low load using neural network. *ISA Transactions* 2016; 64: 241–246.
- [9] Singh G, Naikan VNA. Detection of half broken rotor bar fault in VFD driven induction motor drive using motor square current MUSIC analysis, *Mech Syst Signal Process* 2018; 110: 333–348.
- [10] Ameid T, Menacer A, Talhaoui H, Azzoug Y. Discrete wavelet transform and energy eigen value for rotor bars fault detection in variable speed field-oriented control of induction motor drive. *ISA Transactions* 2018; 79: 217–231.
- [11] Quiroz JC, Mariun N, Mehrjou MR, Izadi M, Misron N, Mohd Radzi MA. Fault detection of broken rotor bar in LS-PMSM using random forests. *Measurement: Journal of the International Measurement Confederation* 2018; 116: 273–280.
- [12] Gandhi P, Turk DN, Dahiya DR. Health monitoring of induction motors through embedded systems-simulation of broken rotor bar fault and abnormal gear teeth fault, *Microprocess Microsyst* 2020; 76.
- [13] Rangel-Magdaleno J, Peregrina-Barreto H, Ramirez-Cortes J, Cruz-Vega I. Hilbert spectrum analysis of induction motors for the detection of incipient broken rotor bars. *Measurement: Journal of the International Measurement Confederation* 2017; 109: 247–255.
- [14] Abd-el-Malek M, Abdelsalam AK, Hassan OE. Induction motor broken rotor bar fault location detection through envelope analysis of start-up current using Hilbert transform, *Mech Syst Signal Process* 2017; 93: 332–350.
- [15] Halder S, Bhat S, Dora BK. Inverse thresholding to spectrogram for the detection of broken rotor bar in induction motor. *Measurement: Journal of the International Measurement Confederation* 2022;198.
- [16] Liu D, Lu D. Off-the-grid compressive sensing for broken-rotor-bar fault detection in squirrel-cage induction motors. *IFAC-PapersOnLine* 2015; 28(21): 1451–1456.
- [17] Georgoulas G, Mustafa MO, Tsoumas IP, Antonino-Daviu JA, Climente-Alarcon V, Stylios CD, Nikolakopoulos G. Principal Component Analysis of the start-up transient and Hidden Markov Modeling for broken rotor bar fault diagnosis in asynchronous machines, *Expert Syst Appl* 2013; 40(17): 7024–7033.
- [18] Khater FMH, Abu El-Sebah MI, Osama M, Sakkoury KS. Proposed fault diagnostics of a broken rotor bar induction motor fed from PWM inverter. *Journal of Electrical Systems and Information Technology* 2016; 3(3): 387–397.
- [19] Meng L, Su Y, Kong X, Xu T, Lan X, Li Y. Intelligent fault diagnosis of gearbox based on differential continuous wavelet transform-parallel multi-block fusion residual network. *Measurement: Journal of the International Measurement Confederation* 2023; 206.
- [20] Wu J da, Chen JC. Continuous wavelet transform technique for fault signal diagnosis of internal combustion engines. *NDT and E International* 2006; 39(4): 304–311.

- [21] Liang P, Wang W, Yuan X, Liu S, Zhang L, Cheng Y. Intelligent fault diagnosis of rolling bearing based on wavelet transform and improved ResNet under noisy labels and environment. *Eng Appl Artif Intell* 2022;115.
- [22] He K, Zhang X, Ren S, Sun J. Deep Residual Learning for Image Recognition, 2015, <http://arxiv.org/abs/1512.03385>.
- [23] Kumar A, Vashishtha G, Gandhi CP, Tang H, Xiang J. Tacho-less sparse CNN to detect defects in rotor-bearing systems at varying speed, *Eng Appl Artif Intell* 2021;104.
- [24] Kang H, Zong X, Wang J, Chen H. Binary gravity search algorithm and support vector machine for forecasting and trading stock indices, *International Review of Economics and Finance* 2023; 84: 507–526.
- [25] Lyu F, Zhou H, Liu J, Zhou J, Tao B, Wang D. A buried hill fault detection method based on 3D U-SegNet and transfer learning, *J Pet Sci Eng* 2022; 218.
- [26] Aline ET, Rogério AF, Marcelo S, Narco ARM. Experimental database for detecting and diagnosing rotor broken bar in a three-phase induction motor, *IEEE Dataport* 2020.
- [27] Mathworks Online Available <https://www.mathworks.com/help/predmaint/ug/broken-rotor-fault-detection-in-ac-induction-motors-using-vibration-and-electrical-signals.html>. Access Date: 12 Nov 2022.
- [28] Turkoglu M, Aslan M, Ari A, Alcin ZM, Hanbay D. A multi-division convolutional neural network-based plant identification system, *Peer J Comput Sci* 2021; 7: p. e572.
- [29] Ari A. Multipath feature fusion for hyperspectral image classification based on hybrid 3D/2D CNN and squeeze-excitation network, *Earth Sci Informatics* 2023; 16: 1–17.
- [30] Donuk K, Ari A, Hanbay D. A CNN based real-time eye tracker for web mining applications, *Multimed Tools Appl* 2022; 81: 1–18.
- [31] Demir F, Sengur A, Ari A, Siddique K, Alswaitti M. Feature Mapping and Deep Long Short Term Memory Network-Based Efficient Approach for Parkinson’s Disease Diagnosis,” *IEEE Access*, 2021; 9: 149456–149464.